Robotica (2022), **40**, pp. 3930–3951
doi:10.1017/S0263574722000686

CAMBRIDGE UNIVERSITY PRESS

RESEARCH ARTICLE

A novel soft-rigid wheeled crawling robot with high payload and passing capability

Jiangming Jia[1], Peilin Cheng[1], Yuze Ye[1], Qizhi Xie[2] and Chuanyu Wu[1,*]

[1]Faculty of Mechanical Engineering and Automation, Zhejiang Sci-Tech University, 310018 Hangzhou, PR China and [2]School of Mechanical and Electrical Engineering, Xuzhou University of Technology, 221018 Xuzhou, PR China
*Corresponding author. E-mail: cywu@zstu.edu.cn

Received: 13 November 2021; **Revised:** 11 March 2022; **Accepted:** 26 April 2022; **First published online:** 8 June 2022

Keywords: soft-rigid wheeled crawling robot, amphibious environment, payload capability, passing capability

Abstract

Soft crawling robots have been significantly studied in recent decades. However, moving in amphibious environment, high payload capability, and passing through complex ground have always been challenges for soft crawling robots. For these problems, this article presents an amphibious soft-rigid wheeled crawling robot (SRWCR) consists of a soft-rigid body actuated by two soft pneumatic actuators (SPAs), four wheels, and four annular soft bladders (ASBs) as brakes. By programming the actuation sequences of the two SPAs and four ASBs, SRWCR can achieve two basic modes of locomotion: linear motion and turning. Based on the energy conservation law, we have developed analytical models to interpret the static actuation performance of SPA, including linear and bending deformations. Furthermore, with the help of fast response and waterproof of SPA and ASB, SRWCR can achieve a linear speed of 14.97 mm/s, a turning speed of 5.63°/s, and an underwater locomotion speed of 13 mm/s, which demonstrates the excellent locomotion performance of SRWCR in amphibious environment. In addition, SRWCR can also achieve multiple impressive functions, including carrying a payload of 2 kg at the moving speed of 11.18 mm/s, passing through various complex ground such as the grass ground and sand ground, and so on, obstacle navigation in confined space. Compared with the existing soft crawling robots, with the help of the soft-rigid body and wheeled structure, SRWCR has the best payload and passing capability, which indicates the potential advantage of SRWCR in the design of functional robots.

1. Introduction

The last decade has witnessed a large impetus in the field of soft robotics, with potential applications in rehabilitation and healthcare, [1] medical invasive surgery, [2] undersea/space search and exploration, [3] food handling, [4] and disaster area survey and rescue. [5] Built of compliant materials, soft robots exhibit muscle-like behavior, resulting in a large number of degrees of freedom. In addition, the soft materials can absorb the energy arising from collisions to keep both the robots and the surroundings safe. Consequently, soft robots can work effectively in unstructured and confined environments. Besides, the inherent compliance can also help soft robots to improve mobility, especially over soft substrates. [6] Unlike the rigid-bodied robots that need complicated mechanical systems to achieve complex movements, soft robots require only simple design and control to generate motions. [7, 8]

Many impressive soft robots inspired by soft-bodied animals such as octopus, [9, 10] caterpillar [11, 12, 13], and jellyfish [14, 15, 16] have been developed in the literature, of which soft crawling robots are particularly interesting due to their potential applications as surveillance robots in complex environments. In the past decade, many kinds of soft crawling robots have been developed with different materials and actuation mechanisms. In particular, as one of the very first soft crawling robots, a quadrupedal soft robot was proposed by Shepherd et al. [17] By combining crawling and undulation paces, this multi-gait robot could navigate difficult obstacles. Later, Tolley et al. [18] developed

an untethered version of this robot, which could work in tough environments. In addition, vacuum-driven pneumatic actuators have been employed in soft crawling robots as well. Qin et al. [19] designed a versatile soft crawling robot actuated by soft pneumatic actuators (SPAs), which can achieve rapid locomotion. Other smart actuators have also been used to develop soft crawling robots, such as shape memory alloys (SMAs), [20] ionic polymer metal composites, [21] magnetorheological fluid, [22] soft electrostatic actuators, [19, 23] as well as dielectric elastomer actuators. [23, 24, 25] However, due to the intrinsic properties of soft materials with low stiffness, the soft bodies of these crawling robots result in low loads, which also limits the payload capacity of these crawling robots. In addition, these soft crawling robots can achieve locomotion on the flat ground either through the mechanism of asymmetric friction or using the adsorption-type actuators as their feet, both of which are not effective when they move on the complex ground such as grass ground, sand road, and mud ground, which leads to their poor passing capacity. On the other hand, because these soft crawling robots are not waterproof or cannot move on complex ground, they are difficult to perform underwater exploration operations.

Recently, some researchers combine rigid structures with soft actuators to increase the load capacity of soft robots. Guo et al. [26] combined the rigid ratchet mechanism with SPA to design a variable stiffness soft-rigid gripper. While not changing the soft contact with the object, the stiffness of the gripper was increased by 20 times, resulting in a significant increase in load. A hybrid robotic gripper with high load has been developed by Su et al. [27] The gripper consisted of rigid skeletons and SPAs. In addition, compared with the soft crawling robots that rely on the mechanism of asymmetric friction or using the adsorption-type actuators as their feet to move, the wheeled robots have better ability to pass through complex ground. [28, 29, 30] Furthermore, because of the intrinsic waterproof of the SPAs, they have been used as actuators for a variety of underwater robots, [31, 32, 33] which have greatly simplified the structure of underwater robots and saved the manufacturing costs.

In this article, inspired by the high load of soft-rigid structure, the high passing capacity of wheeled robot, and the waterproof of SPAs, we developed an amphibious soft-rigid wheeled crawling robot (SRWCR) that consists of a soft-rigid body actuated by two SPAs, four wheels and, four annular soft bladders (ASBs) as brakes. The simple structure of the SPA allows for the development of analytical models, which can be used to interpret the actuation performance of the robot. Furthermore, the fast and stable locomotion in the air and underwater indicates the excellent locomotion performance of the SRWCR in amphibious environment. Finally, compared with the existing soft crawling robots, the soft-rigid body and wheeled structure make the SRWCR have the best payload and passing capability, so that the SRWCR has inherent advantage in the design of functional robots.

The rest of this article is described as follows: in Section 2, the design and locomotion mechanism of the SRWCR are described. In Section 3, the theoretical models of the linear and bending deformation of the SRWCR are established. The linear and turning speed of the SRWCR are measured in Section 4. The capabilities of the SRWCR are explored in Section 5, before conclusions and future work presented in Section 6.

2. Materials and methods

2.1. Mechanical design of SRWCR

As shown in Fig. 1(a), the proposed SRWCR mainly consists of a rigid head and tail connected by two SPAs as the robot body, four rigid wheels as the robot feet, and four ASBs as the brakes. The front and rear ends of SPAs are, respectively, fixed with rigid connectors to facilitate connection with the rigid head and tail. In addition, four silicone rings with jagged texture on the cylindrical surface are fixed on the four rigid wheels to increase the friction between the wheels and the ground. The rigid head, tail, wheels, and two connectors are fabricated by 3D printing (ABS, F170, Stratasys). As shown in Fig. 1(b), SPA manufactured by the mold casting method [34] is composed of a metal spring wound on the outer wall of a soft cylinder made of silicone rubber (Tianying950, Dongguan Tianying Craft Material Co., Ltd). The specification of the spring is shown in Table I. A thin air tube is employed to connect the cavity of the silicone cylinder with an air compressor for pneumatic actuation. Upon pressure, the spring restrains

https://doi.org/10.1017/S0263574722000686 Published online by Cambridge University Press

Table I. *Specification of the metal spring.*

Spring parameter	Value
Material	SUS304WPB
Wire diameter	0.75 mm
Outside diameter	20.0 mm
Pitch	1.0 mm

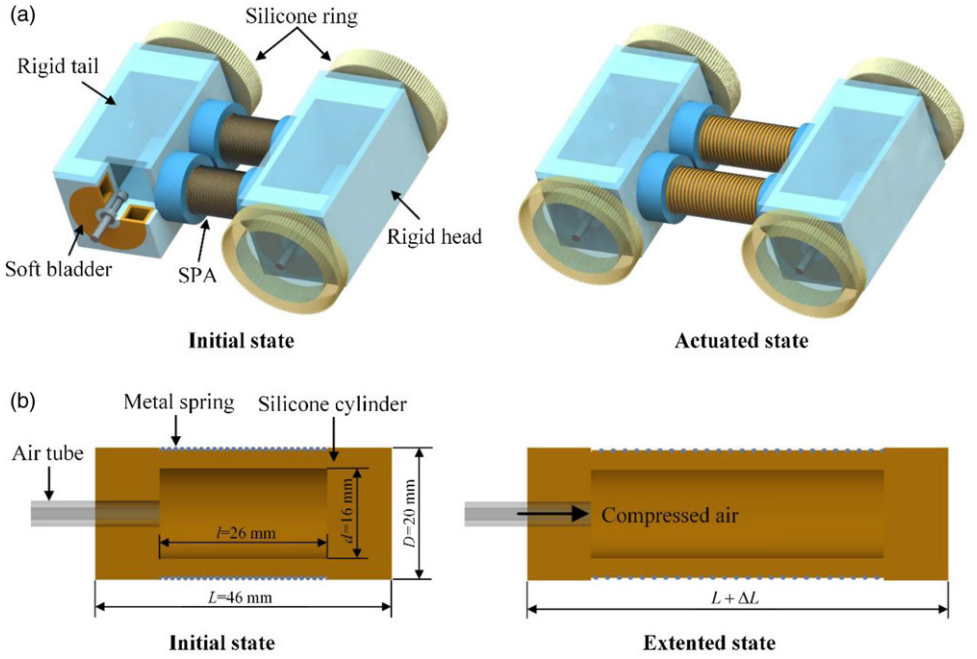

Figure 1. *Schematic of SRWCR and SPA. (a) SRWCR consists of a soft-rigid body actuated by two SPAs, four wheels, and four annular soft bladders as brakes. (b) SPA consists of a metal spring wound on the outer wall of the soft cylinder.*

the expansion of the silicone cylinder in radial direction and fixes the extension direction of SPA in axial direction. The axial extension of SPA can push the wheels to rotate forward/backward which are installed on the rigid head and tail by stainless steel shafts and waterproof bearings (SMR74ZZ, NSK). After depressurization, SPA will contract to the initial state.

Besides the SPAs, the four ASBs made of silicone rubber (Tianying950, Dongguan Tianying Craft Material Co., Ltd) play an important role in achieving the fundamental locomotion modes (linear and turning motion) of SRWCR. As shown in Fig. 1(a), the four ASBs are fixed in the annular grooves at both ends of the rigid head and tail, respectively. Because the annular groove encloses the inner wall and two side walls of the ASB, the outer wall of the bladder is exposed in the free space. A thin air tube is employed to connect the ASB with an air compressor for pneumatic actuation. Upon pressure, the expansion of outer wall of the ASB can brake the corresponding wheel. After depressurization, the ASB will return to its initial state. To increase the friction between the outer wall of the ASB and the wheel, sandpaper with large roughness is glued on the wheel.

2.2. Locomotion mechanism

In order to achieve the two fundamental locomotion modes (linear and turning motion) of SRWCR, the two SPAs and four ASBs need to be actuated with different sequences. Figure 2 shows the actuation

https://doi.org/10.1017/S0263574722000686 Published online by Cambridge University Press

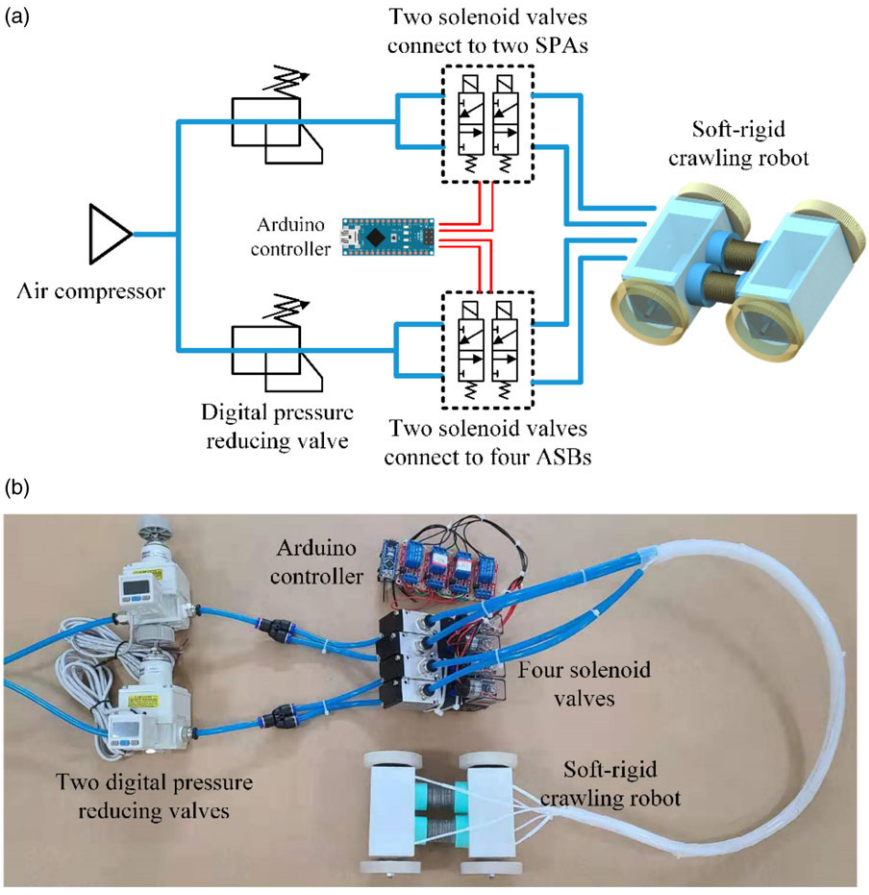

Figure 2. *Experimental apparatus for air supply and control system of SRWCR. (a) Schematic of the air supply and control system. (b) Air supply and control system used in the experiments.*

device that can realize different actuation sequences of SPAs and ASBs. The air compressor supplies compressed air to SPAs and ASBs by connecting digital pressure reducing valves (IR2000, Atuosi) and solenoid valves (N3V210, CHNT) in turn through flexible air tubes. Two digital pressure reducing valves can independently adjust the output pressure of the air compressor to avoid the burst of SPAs and bladders caused by excessive pressure. The solenoid valves can be used as actuation switches of SPAs and bladders. According to the actuation sequences of SPAs and bladders described in detail below, the two SPAs are connected to two solenoid valves so that they can be actuated independently. The two front ASBs are connected to a solenoid valve so that they can be actuated simultaneously. Similarly, the two rear ASBs are connected to a solenoid valve. The switching sequences of the four solenoid valves are controlled by an Arduino controller (Arduino Nano) to achieve the linear and turning motion of SRWCR.

As shown in Fig. 3(a), the actuation sequence of SPAs and ASBs which achieves the linear motion of SRWCR involves four steps: (1) the two rear ASBs are activated simultaneously to brake the corresponding wheels so that they cannot move backward during the extension of SPAs in step (2). (2) Both SPAs extend simultaneously to push the two front wheels to move forward. (3) The two front ASBs are activated simultaneously to prevent the corresponding wheels from moving backward after the contraction of the two SPAs in step (4). (4) The two rear ASBs are deactivated simultaneously, at the same time, the two SPAs contract to pull the two rear wheels to move forward. Repeating the actuation sequence, SRWCR will move forward continuously. Figure 3(b) schematically demonstrates the movement of the SRWCR by following this actuation sequence in Fig. 3(a).

https://doi.org/10.1017/S0263574722000686 Published online by Cambridge University Press

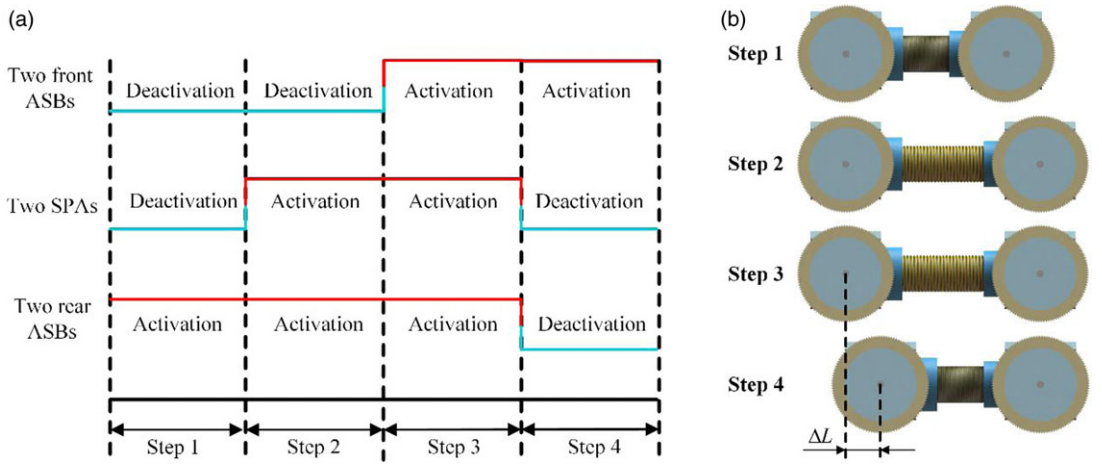

Figure 3. *Actuation sequence and moving step for linear motion of SRWCR. (a) Actuation sequence of the two SPAs, two front ASBs, and two rear ASBs. The red line indicates that the actuator is actuated, whereas the blue line indicates that the actuator is unactuated. (b) Schematic of the forward locomotion of SRWCR by following the actuation sequence in (a).*

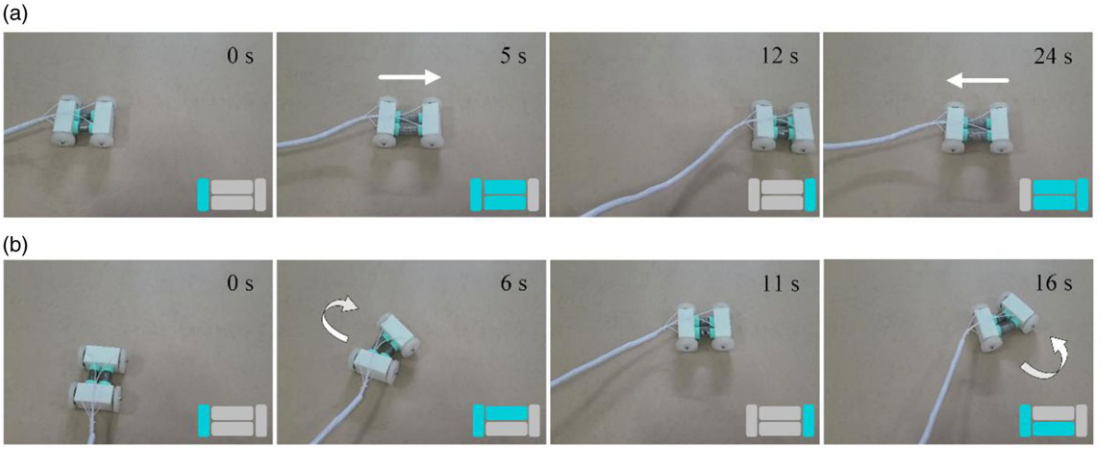

Figure 4. *Demonstration of the two basic modes of locomotion. (a) A sequence of images of SRWCR crawling in two directions. The arrows indicate the direction of motion. (b) A sequence of images of SRWCR turning in two directions. The arrows indicate the direction of motion. The cyan rectangles on the insets (at the bottom right corner) indicate which actuators are currently actuated; gray rectangles represent deactivation of the actuators.*

Furthermore, the linear motion direction of SRWCR is determined by the braking sequence of the two front and two rear wheels. SRWCR is capable of moving toward another direction by simply reversing the braking sequence of the two front and two rear wheels (i.e., exchanging step (1) and step (3) of the actuation sequence). Figure 4(a) shows a sequence of images when SRWCR achieves forward and backward movement. The small schematic inset at the bottom right corner of each frame indicates the actuation states of the actuators at the corresponding step. A video showing the bidirectional linear motion of the robot is available in Supplementary Movie S1.

In addition to linear movement, this soft robot can also achieve turning motion. When both SPAs are actuated, SRWCR can achieve linear motion, as discussed earlier. However, when only one of SPAs is

https://doi.org/10.1017/S0263574722000686 Published online by Cambridge University Press

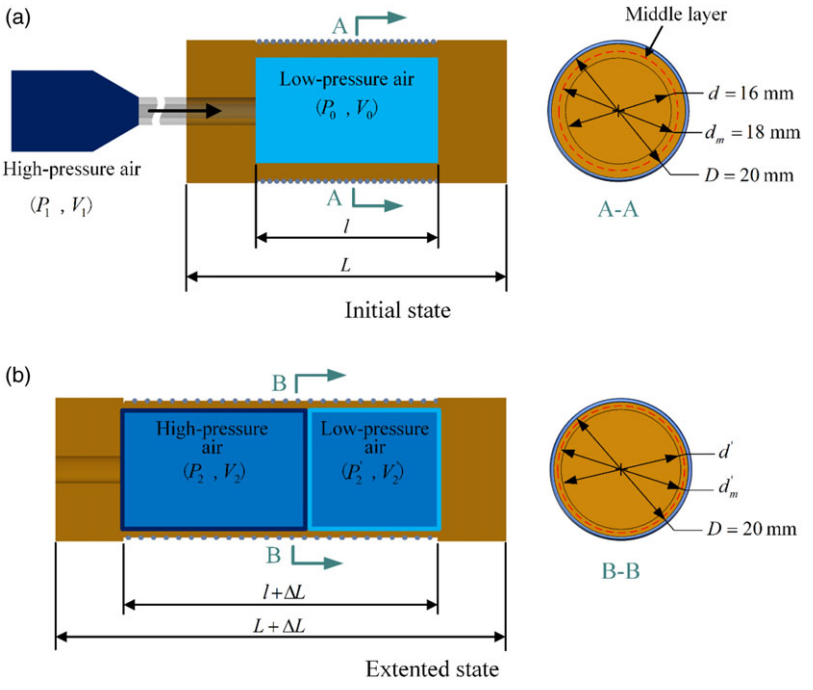

Figure 5. *Schematic of the actuation state of SPA. (a) Initial state: the high-pressure air is not supplied into the cavity of SPA. (b) Actuated state: SPA is actuated by the high-pressure air.*

actuated, SRWCR turns due to the constraint imposed by the other SPA. The detailed turning performance will be discussed later. The actuation sequences for the turning motion are similar to those of the linear motion in Fig. 3(a) except that only one SPA is actuated. For example, by following the actuation sequences in the insets of Fig. 4(b), SRWCR turns clockwise when only the left SPA is activated. Similarly, SRWCR turns anticlockwise by actuating the right SPA only while keeping the actuation signals unchanged for the front and rear soft bladders. Supplementary Movie S2 demonstrates the turning motion of SRWCR. Figure 4(b) shows the captured images of SRWCR from this turning motion. SRWCR first makes a clockwise turn and then reserves the turning direction.

3. Theoretical modeling of SPA

As mentioned earlier, the deformation of the two SPAs which act as the soft body of SRWCR determines the characteristic of linear and bending motion of SRWCR. In addition, the deformation of SPA depends on the input air pressure. In this section, analysis modeling is established to understand the relation between the input air pressure and the corresponding deformation.

3.1. Linear deformation

For linear deformation, both SPAs exhibit identical deformation under the same actuation pressure; hence, only one actuator is considered in this section to analyze the extension length ΔL upon air pressure ΔP. Figure 5(a) shows that the SPA is in the initial state before it is actuated by the high-pressure air shown by the dark blue area. The pressure of the low-pressure air shown by the light blue area in the cavity of the SPA is a standard air pressure ($P_0 \approx 0.1$ MPa). When the high-pressure air is supplied into the cavity, as shown in the dark blue box in Fig. 5(b), the volume of high-pressure air expands from V_1 to V_2, and its pressure drops from P_1 to P_2. Meanwhile, the expanded high-pressure air does work to the low-pressure air in the cavity, silicone cylinder, and spring. Therefore, as shown by the light blue box in

https://doi.org/10.1017/S0263574722000686 Published online by Cambridge University Press

Fig. 5(b), the volume of the low-pressure air is compressed from V_0 to V_2', and its pressure rises from P_0 to P_2'. The extension length of SPA is ΔL. If the energy dissipation in the process of actuating the SPA is ignored, according to the energy conservation law, the following relation can be obtained:

$$W_1 = W_0 + W_2 + W_3 \tag{1}$$

where W_1 is the work done by the expansion of the high-pressure air from initial state to extended state of SPA, W_0 is the energy absorbed by the compression of the low-pressure air from initial state to extended state of SPA, W_2 is the strain energy of the silicone cavity in the extended state, and W_3 is the elastic potential energy of the spring.

We assume that the high-pressure air and low-pressure air in Fig. 5(a) are ideal gas. The expansion process of the high-pressure air and the compression process of the low-pressure air in Fig. 5(b) are adiabatic and isentropic. Therefore, the high-pressure air in expansion process and the low-pressure air in compression process satisfy the relation in Eqs. (2) and (3), respectively. Equations (2) and (3) are described as follows:

$$PV^r = P_1V_1^r = P_2V_2^r \tag{2}$$

and

$$P'V'^r = P_0V_0^r = P_2'V_2'^r \tag{3}$$

where P and V are the pressure and volume, respectively, of the high-pressure air at any time during the expansion process, P_1 and V_1 are the pressure and volume, respectively, of the high-pressure air in the initial state, P_2 and V_2 are the pressure and volume, respectively, of the high-pressure air in the extended state, r is the polytropic coefficient which is a constant ($r = 1.4$), P' and V' are the pressure and volume, respectively, of the low-pressure air at any time during the compression process, P_0 and V_0 are the pressure and volume, respectively, of the low-pressure air in the initial state, and P_2' and V_2' are the pressure and volume, respectively, of the low-pressure air in the extended state.

In the extended state shown in Fig. 5(b), the expanded high-pressure air and the compressed low-pressure air are in equilibrium in the cavity of SPA. Therefore, the following relation can be obtained:

$$P_2 = P_2' \tag{4}$$

Furthermore, the work W_1 done by the expansion of the high-pressure air and the energy W_0 absorbed by the compression of the low-pressure air satisfy the relation in Eqs. (5) and (6), respectively. Equations (5) and (6) are described as follows:

$$W_1 = \int_{V_1}^{V_2} PdV \tag{5}$$

And

$$W_0 = \int_{V_2'}^{V_0} P'dV' \tag{6}$$

The volume relation between the expanded high-pressure air and compressed low-pressure in Fig. 5(b) is expressed as:

$$V_2 = V_0 + \frac{\pi \Delta L d^2}{4} - V_2' \tag{7}$$

where ΔL is the extension length of SPA in extended state and d is the inner diameter of the silicone cylinder.

Substituting Eqs. (2), (4), and (7) into Eq. (5), the work W_1 done by the expansion of the high-pressure air is expressed as:

$$W_1 = \frac{\left(P_2 - P_2^{\frac{1}{r}}P_1^{\frac{r-1}{r}} - \left(P_2^{\frac{r-1}{r}} - P_1^{\frac{r-1}{r}}\right)P_0^{\frac{1}{r}}\right)V_0 + \frac{\pi \Delta L d^2}{4}\left(P_2 - P_2^{\frac{1}{r}}P_1^{\frac{r-1}{r}}\right)}{1-r} \tag{8}$$

https://doi.org/10.1017/S0263574722000686 Published online by Cambridge University Press

Furthermore, substituting Eqs. (3) and (4) into Eq. (6), the energy W_0 absorbed by the compression of the low-pressure air is described as:

$$W_0 = \frac{\left(P_0 - P_0^{\frac{1}{r}} P_2^{\frac{r-1}{r}}\right) V_0}{1-r} \tag{9}$$

Because P_2 is the absolute pressure in the cavity of SPA in extended state, the relation between the relative pressure ΔP and the absolute pressure P_2 in the cavity is $P_2 = \Delta P + P_0$. Substituting this relation into Eqs. (8) and (9), respectively, W_1 and W_0 can be expressed as:

$$W_1 = \frac{\left((\Delta P + P_0) - (\Delta P + P_0)^{\frac{1}{r}} P_1^{\frac{r-1}{r}} - \left((\Delta P + P_0)^{\frac{r-1}{r}} - P_1^{\frac{r-1}{r}}\right) P_0^{\frac{1}{r}}\right) V_0}{1-r} + \frac{\frac{\pi \Delta L d^2}{4}\left((\Delta P + P_0) - (\Delta P + P_0)^{\frac{1}{r}} P_1^{\frac{r-1}{r}}\right)}{1-r} \tag{10}$$

and

$$W_0 = \frac{\left(P_0 - (\Delta P + P_0)^{\frac{r-1}{r}} P_0^{\frac{1}{r}}\right) V_0}{1-r} \tag{11}$$

In addition to compressing the low-pressure air, the expansion of the high-pressure air also drives SPA to extend in Fig. 5(b). Therefore, part of the work done by the expansion of the high-pressure air is converted into the strain energy W_2 of the cylindrical silicone wall and the elastic potential energy W_3 of the spring. The strain energy W_2 of the silicone wall satisfies the following relation:

$$W_2 = W V_s \tag{12}$$

where W is the volumetric energy density of the silicone rubber and V_s is the volume of the silicone wall which can be expressed as:

$$V_s = \frac{\pi\left(D^2 - d^2\right) l}{4} \tag{13}$$

where D and d are the outer diameter and inner diameter, respectively, of the silicone cylinder and l is the length of the cavity of SPA.

Mooney–Rivilin model is often used to predict the nonlinear and large deformation of the silicone rubber. [35] Here, we used this model to calculate the volumetric energy density W of the silicone rubber. The Mooney–Rivilin model is given as:

$$W = C_{10}(I_1 - 3) + C_{01}(I_2 - 3) \tag{14}$$

where C_{10} and C_{01} are the material constants with the value of 0.1064 and 0.0019 MPa, respectively, which were measured by a tensile test (ZQ-1000, China). I_1 and I_2 are the first and second principal invariants of the Cauchy–Green strain tensor, which can be expressed as:

$$\begin{cases} I_1 = \lambda_r^2 + \lambda_\theta^2 + \lambda_a^2 \\ I_2 = \lambda_r^2 \lambda_\theta^2 + \lambda_\theta^2 \lambda_a^2 + \lambda_a^2 \lambda_r^2 \end{cases} \tag{15}$$

where λ_r, λ_θ, and λ_a are the radial elongation ratio, circumferential elongation ratio and axial elongation ratio, respectively, of the silicone wall.

While SPA is actuated by the high-pressure air, the spring wound on the outer wall of the silicone cylinder restrains its radial expansion. Therefore, the outer diameter D of the silicone cylinder remains unchanged. However, the inner diameter of the silicone cylinder increases with the increase of the extension length.

As shown in Fig. 5(a) and (b), when the length of the cylindrical silicone wall is extended from l to $l + \Delta L$, the inner diameter of the silicone cylinder increases from d to d'. The red dash circles shown in

https://doi.org/10.1017/S0263574722000686 Published online by Cambridge University Press

the section views of Fig. 5(a) and (b) represent the middle layer of the silicone wall in the initial state and extended state, respectively. Because the thickness (t=2 mm) of the silicone wall in the initial state is much smaller than the outer diameter (D=20 mm) of the silicone cylinder, we regard the circumferential elongation ratio of the middle layer as the circumferential elongation ratio of the silicone wall during the extension of SPA. Then, the thickness change ratio and length change ratio of the silicone wall can be considered as the radial elongation ratio and axial elongation ratio of the silicone wall, respectively. Therefore, the radial elongation ratio λ_r, circumferential elongation ratio λ_θ, and axial elongation ratio λ_a of the silicone wall in the extended state shown in Fig. 5(b) can be expressed as:

$$\begin{cases} \lambda_r = \dfrac{D - d'}{D - d} \\ \lambda_\theta = \dfrac{\pi d'_m}{\pi d_m} = \dfrac{D + d'}{D + d} \\ \lambda_a = \dfrac{l_1}{l} = \dfrac{l + \Delta L}{l} \end{cases} \tag{16}$$

where d_m and d'_m are the diameters of the middle layer in the initial state and extended state, respectively. According to the incompressibility of the silicone rubber, we have the following relation:

$$\lambda_r \lambda_\theta \lambda_a = 1 \tag{17}$$

Substituting Eqs. (13), (14), (15), (16), and (17) into Eq. (12), the strain energy W_2 of the silicone wall in the extended state can be obtained:

$$W_2 = \frac{\pi C_{10}\left(D^2 - d^2\right)}{4}\left(\frac{2l^2}{l + \Delta L} + \frac{(l + \Delta L)^2}{l} - 3\right) + \frac{\pi C_{01}\left(D^2 - d^2\right)}{4}\left(\frac{l^3}{(l + \Delta L)^2} + 2(l + \Delta L) - 3\right) \tag{18}$$

Furthermore, the elastic potential energy W_3 of the spring under the extension length ΔL can be expressed as:

$$W_3 = \frac{k\Delta L^2}{2} \tag{19}$$

where k is the stiffness coefficient of the metal spring with a value of 50 N/m, which was measured by a tensile test (ZQ-100, China).

Substituting Eqs. (10), (11), (18), and (19) into Eq. (1), the relation between the extension length ΔL of SPA and the pressure ΔP in the cavity of the silicone cylinder can be obtained:

$$\begin{aligned} &\frac{\left(\Delta P + \left(P_0^{\frac{1}{r}} - (\Delta P + P_0)^{\frac{1}{r}}\right)P_1^{\frac{r-1}{r}}\right)V_0 + \dfrac{\pi \Delta L d^2}{4}\left((\Delta P + P_0) - (\Delta P + P_0)^{\frac{1}{r}} P_1^{\frac{r-1}{r}}\right)}{1 - r} - \frac{1}{2}k\Delta L^2 \\ &- \frac{\pi C_{10}\left(D^2 - d^2\right)}{4}\left(\frac{2l^2}{l + \Delta L} + \frac{(l + \Delta L)^2}{l} - 3\right) + \frac{\pi C_{01}\left(D^2 - d^2\right)}{4}\left(\frac{l^3}{(l + \Delta L)^2} + 2\,(l + \Delta L) - 3\right) = 0 \end{aligned} \tag{20}$$

To verify the analytical model of the linear deformation of SPA, we conducted experiments to measure the extension length ΔL at different pressures ΔP. The experimental setup is shown in Fig. 6(a). SPA was fixed on the optical platform by a support frame fabricated by 3D printing. The extension length ΔL of SPA was measured by a digital laser displacement sensor (BL-100N, BOJKE) located on the left side of SPA. The pressure ΔP of the compressed air supplied by an air compressor was adjusted by a digital pressure reducing valve (IR2000, Atuosi). To prevent the burst of SPA, a pretest has been carried out to determine that the maximum pressure supplied to SPA is 0.2 MPa. The pressure was supplied to SPA from 0 to 0.2 MPa with a step size of 0.01 MPa. Ten trials were conducted under the same conditions to confirm the repeatability. The average measurement results are plotted in Fig. 6(b).

Figure 6(b) shows the comparison between the theoretical (black line) and experimental (red circles) results for the extension length at different pressures. The error bar represents the standard deviation of

https://doi.org/10.1017/S0263574722000686 Published online by Cambridge University Press

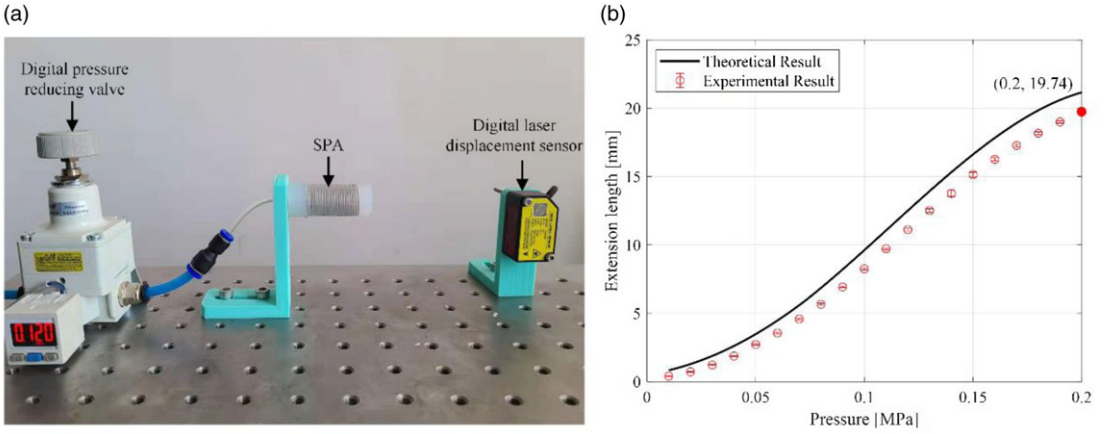

Figure 6. *Measurement of the extension length of SPA under different pressures. (a) Experimental apparatus used in the measurement. (b) Comparison between the theoretical and experimental results for the extension length of SPA under different pressures.*

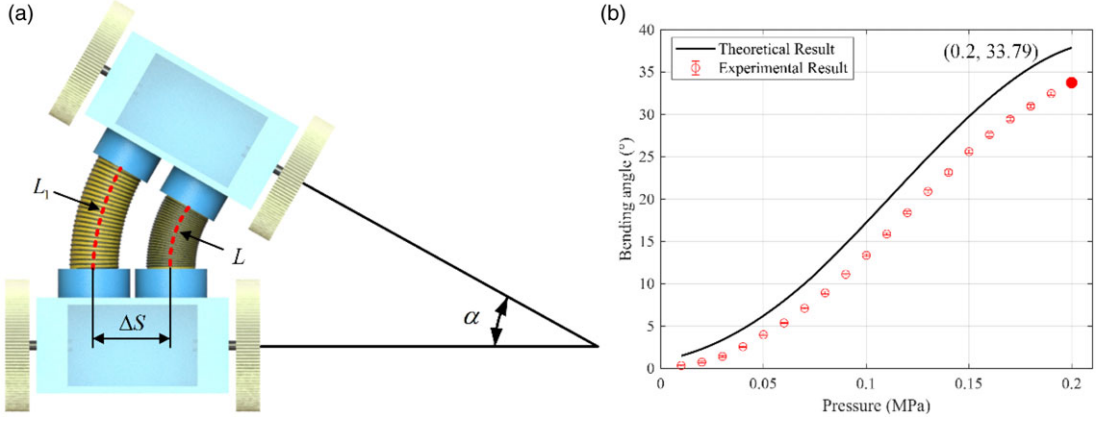

Figure 7. *Measurement of the bending deformation of SPA. (a) Schematic of the bending deformation of SPA. (b) Comparison between the theoretical and experimental results for the bending angle of SPA under different pressures.*

10 measurements of the extension length at each pressure. With the increase of pressure, the theoretical extension length and experimental extension length both show a nonlinear increasing trend because of the nonlinear deformation of the silicone rubber. It is clear that the maximum extension length of SPA is 19.74 mm at the pressure of 0.2 MPa. The theoretical results agree well with the experimental results. However, the discrepancy between the theoretical result and the experimental result increases with the increase of the pressure. There are two main reasons: (1) there is energy dissipation during the extension of SPA actuated by the high-pressure air, which increases with the increase of the pressure, and (2) the thickness of the silicone wall casting in the lab is not completely uniform, which leads to slight bending deformation during the extension of SPA, and the bending deformation of SPA increases with the increase of the pressure.

3.2. Bending deformation

As described in Section 2.2, when only one SPA is actuated, this SPA will bend due to the constraint of another SPA, which drives SRWCR to turn. As shown in Fig. 7(a), the actuated left SPA bends an angle

https://doi.org/10.1017/S0263574722000686 Published online by Cambridge University Press

α to the right due to the constraint of the right SPA. Meanwhile, the right SPA is forced to bend the same angle to the right by the left SPA. Because the right SPA is only forced to bend and is not actuated by the high-pressure air, we consider the length of the centerline of the right SPA remains unchanged. The length of the centerline of the left SPA is L_1. From Fig. 7(a), the following geometric relation can be obtained:

$$\frac{L_1 - L}{\alpha} = \Delta s \tag{21}$$

where Δs is the distance between the centerlines of the two SPAs. In addition, we assume that the previous relation for linear deformation still holds during bending motion. Then, we know that $L_1 = L + \Delta L$, where ΔL is the extension length of the centerline of the left SPA under the pressure of ΔP. By substituting this relation into Eq. (21), we have

$$\Delta L = \alpha \Delta s \tag{22}$$

Substituting Eq. (22) into Eq. (20), the relation between the bending angle α and the input pressure ΔP can be expressed as:

$$\frac{\left(\Delta P + \left(P_0^{\frac{1}{r}} - (\Delta P + P_0)^{\frac{1}{r}}\right) P_1^{\frac{r-1}{r}}\right) V_0 + \frac{\pi \Delta L d^2}{4}\left((\Delta P + P_0) - (\Delta P + P_0)^{\frac{1}{r}} P_1^{\frac{r-1}{r}}\right)}{1 - r} - \frac{1}{2} k \alpha^2 \Delta s^2$$
$$- \frac{\pi C_{10}\left(D^2 - d^2\right)}{4}\left(\frac{2l^2}{l + \alpha \Delta s} + \frac{(l + \alpha \Delta s)^2}{l} - 3\right) + \frac{\pi C_{01}\left(D^2 - d^2\right)}{4}\left(\frac{l^3}{(l + \alpha \Delta s)^2} + 2\,(l + \alpha \Delta s) - 3\right) = 0 \tag{23}$$

Experiment on bending angles at different pressures was conducted to validate the bending model. The two rear wheels were braked by the two rear ASBs, and the left SPA was actuated. The pressure was applied from 0 to 0.2 MPa with a step size of 0.01 MPa. At each pressure, the bending angle was obtained using image analysis software (Image J, National Institute of Health, MD). Ten trials were conducted under the same conditions to confirm the repeatability. The average results are shown in Fig. 7(b).

Figure 7(b) shows the comparison between the theoretical (black line) and experimental (red circles) results for the bending angle at different pressures. The error bar represents the standard deviation of 10 measurements of the bending angle at each pressure. It is obvious that the maximum bending angle of SPA is 33.79° at the pressure of 0.2 MPa. In addition, with the increase of the pressure, the increasing trend of the theoretical bending angle is consistent with that of the experimental bending angle. However, the discrepancy between the theoretical result and the experimental result increases with the increase of the pressure. The main reason is that because of the constraint of the unactuated SPA, the extension length of the centerline of the actuated SPA in the experiment is less than the theoretical value, and the discrepancy between them increases with the increase of the pressure.

4. Measurement of the linear and turning speed

The input pressure of SPA and the actuation period of SRWCR are two main factors that affect the linear and turning speed of SRWCR. As discussed earlier in Figs. 6(b) and 7(b), larger input pressure leads to larger linear and bending deformation of SPA. Therefore, the pressure of 0.2 MPa is supplied into SPA to achieve larger linear and turning speed of SRWCR. The actuation period of SRWCR is defined as the time taken to achieve one actuation sequence of the linear motion or turning motion of SRWCR. Because the only difference between the actuation sequences of the turning motion and linear motion is that only one of SPAs is actuated in turning motion, the turning motion and linear motion have the same actuation period. In this section, we mainly focus on measuring the actuation period to measure the linear and turning speed of SRWCR.

https://doi.org/10.1017/S0263574722000686 Published online by Cambridge University Press

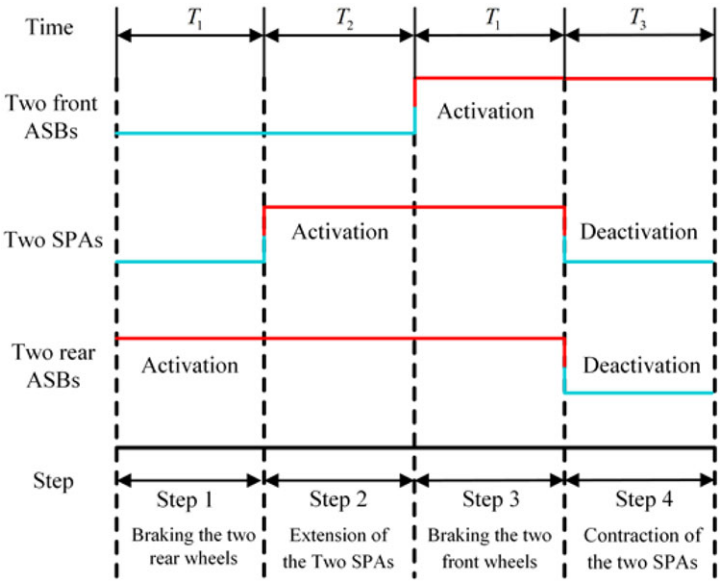

Figure 8. *Schematic of the actuation period for the linear motion of SRWCR. The actuation period includes the braking time of the two front wheels and the two rear wheels, as well as the extension time and contraction time of the two SPAs.*

4.1. Measurement of the actuation period

We take the linear motion of SRWCR as an example to analyze the actuation period of SRWCR. Because the actuation sequence of the linear motion involves four steps shown in Fig. 3(a), the actuation period is equal to the total time taken to achieve the four steps. As shown in Fig. 8, the actuation period T of the linear motion can be obtained:

$$T = 2T_1 + T_2 + T_3 \tag{24}$$

where T_1 is the braking time taken by ASB to brake the wheel, and T_2 and T_3 are the extension time and contraction time of SPA, respectively.

An experiment has been conducted to measure the extension time T_2 and contraction time T_3 of SPA. The experimental setup is shown in Fig. 9(a). The SPA was fixed on the optical platform by a support frame fabricated by 3D printing. The extension length ΔL of the SPA was measured by a digital laser displacement sensor (BL-100N, BOJKE), and the data were collected with a sampling frequency of 100 Hz through a data acquisition device (USB-6002, National Instrument). The compressed air was supplied into SPA by connecting a digital pressure reducing valve and a solenoid valve in turn through flexible air tubes. The solenoid valve used as the actuation switch of SPA was controlled by an Arduino controller (Arduino Nano). Before the experiment, the pressure of the compressed air was adjusted to 0.2 MPa by the digital pressure reducing valve. Then, the solenoid valve was opened under the control of the Arduino controller, and SPA began to extend. After the solenoid valve was opened for 1.5 s which is much longer than the extension time of SPA, the solenoid valve was closed, and SPA began to contract. The extension length of SPA during the extension and contraction processes were recorded by the data acquisition device. Three trials were conducted under the same conditions to confirm the repeatability. The average measurement results are plotted in Fig. 9(b). The full extension phase (rising) between the two blue dash line takes about 0.4 s to reach the maximum extension length, and the contraction phase (dropping) between the two red dash line takes about 0.5 s. Therefore, the extension time T_2 and contraction time T_3 of SPA are 0.4 and 0.5 s, respectively.

https://doi.org/10.1017/S0263574722000686 Published online by Cambridge University Press

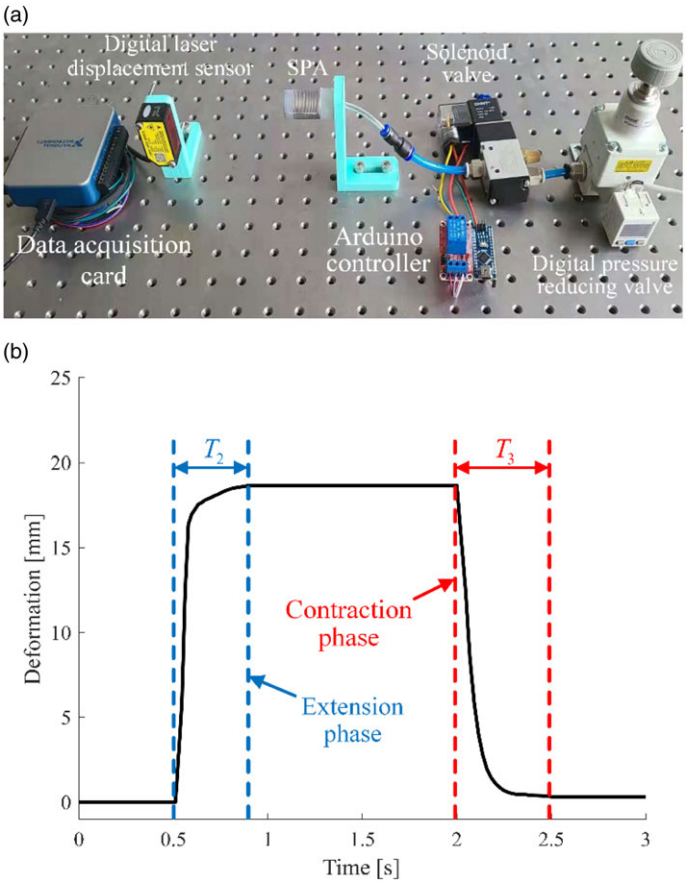

Figure 9. *Measurement of the extension time and contraction time of SRWCR. (a) Measuring device for the extension time and contraction time of SRWCR. (b) The deformation curve of SPA actuated by the pressure of 0.2 MPa. The extension phase between the two blue dash line takes about 0.4 s. The contraction phase between the two red dash line takes about 0.5 s.*

Before measuring the braking time of ASB, to prevent ASB from bursting due to the excessive pressure, the safety pressure supplied to ASB has been measured which is 0.08 MPa. Then, the same experimental setup shown in Fig. 2 was employed to determine the braking time of ASB. The pressures supplied to ASB and SPAs were adjusted to 0.08 and 0.2 MPa, respectively. The two rear wheels were braked by the corresponding ASBs. Then, after a delay, the two SPAs were extended simultaneously. If the two rear wheels could not move backward during the extension of SPAs, we considered that they were fully braked. The experimental result indicates that when the delay time is ≥ 0.15 s, the two rear wheels can be fully braked. Therefore, the braking time of ASB is 0.15 s. Substituting the braking time T_1, extension time T_2, and contraction time T_3 into Eq. (24), the actuation period of SRWCR (T=1.2 s) can be obtained.

4.2. Measurement of the linear speed

The same experimental setup shown in Fig. 2 was employed to measure the linear speed of SRWCR crawling on the flat ground. The pressures supplied to SPAs and ASBs were adjusted to 0.2 and 0.08 Mpa, respectively, by the two digital pressure reducing valves. The braking time of ASB and the extension time and contraction time of SPA were set to 0.15, 0.4, and 0.5 s, respectively, to ensure that the actuation

https://doi.org/10.1017/S0263574722000686 Published online by Cambridge University Press

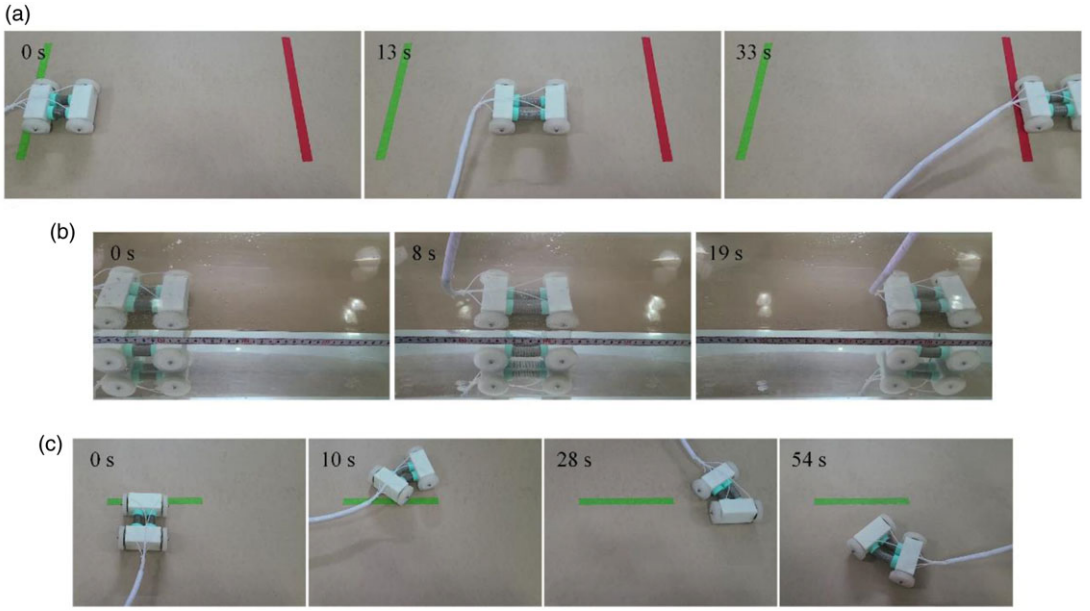

Figure 10. *Measurement of the motion speed of SRWCR. (a) The image snapshots of the linear speed measurement of SRWCR. (b) The image snapshots of the underwater locomotion process of SRWCR. (c) The image snapshots of the turning speed measurement of SRWCR.*

period of SRWCR is 1.2 s. SRWCR crawled from the green start line to the red finish line with a crawling distance of 500 mm. The linear crawling process shown in Supplementary Movie S3 was recorded by a camera. Figure 10(a) shows the snapshots of the linear crawling process. Three trials were conducted under the same conditions to calculate the average crawling speed. The experimental results show that the average linear speed of SRWCR is 14.97 mm/s.

In addition to moving in the air, the intrinsic waterproof of SPAs and ASBs allows SRWCR to move underwater. Except for moving at the bottom of a glass water tank, the measurement experiments of the linear speed of SRWCR moving underwater and in the air have the same experimental configuration. The underwater crawling process of SRWCR shown in Supplementary Movie S4 was recorded by a camera. Figure 10(b) shows the snapshots of the underwater crawling process. Three trials were conducted under the same conditions to calculate the average underwater crawling speed. The experimental results show that the average underwater linear speed of SRWCR is 13 mm/s, which is smaller than the linear speed in the air due to the resistance of water.

4.3. Measurement of the turning speed

In addition to measuring the linear speed, we have conducted an experiment to measure the turning speed of SRWCR. The experimental setup is the same as the experimental setup shown in Fig. 2. Similar to the linear speed measurement experiment, the pressures supplied to SPAs and ASBs were adjusted to 0.2 and 0.08 MPa, respectively, and the actuation period of SRWCR was set to 1.2 s. SRWCR started from the green start line and turned clockwise to return to the green start line. The turning process of SRWCR shown in Supplementary Movie S5 was recorded by a camera. Figure 10(c) shows the snapshots of the turning process. Three trials were conducted under the same conditions to calculate the average crawling time. The experimental results show that the average crawling time is 64 s, and the turning speed of the SRWCR is 5.63°/s. In addition, the rotation center almost remains in the same place, which can be observed from Supplementary Movie S5, and the turning diameter of SRWCR is about 150 mm.

https://doi.org/10.1017/S0263574722000686 Published online by Cambridge University Press

Table II. *Comparison of the performance of our robot with existing soft crawling robots.*

Soft crawling robot	Actuation method	Turning speed (°/s)	Linear speed (mm/s)	Crawling underwater
Our robot	Pneumatic	5.63	14.97	Yes
Zou et al. [11]	Pneumatic	∼ 1.63	5.14	Not report
Tolley et al. [18]	Pneumatic	0.2	5	Not report
Dong et al. [36]	Pneumatic	3.61	13.98	Not report
Jiang et al. [37]	Pneumatic	–	2.5	Not report
Ge et al. [38]	Pneumatic	–	8.9	Not report
Qin et al. [19]	Vacuum	15.09	16.29	Not report
Liang et al. [20]	SMA	–	1.91	No
Tang et al. [39]	Nickel wire	–	1.2	No
Cao et al. [23]	DE	–	4.16	No

Table II shows a comparison of the performance of our robot with existing soft crawling robots. Among the crawling robots in Table II, only the robot developed by Qin et al. [19] has a larger linear speed and turning speed than our robot, which demonstrates that our robot has excellent locomotion performance. In addition, only our robot has the underwater locomotion capability. This capability mainly lies in the waterproof of SPAs and ASBs of our robot. The underwater locomotion capability also indicates the potential advantage of our robot in the design of highly efficient underwater robots, such as underwater sampling robots, underwater monitoring robots, and underwater archaeological robots.

5. Capabilities of the SRWCR

The use of soft-rigid structure as robot body and rigid wheels as feet makes SRWCR to not only have a high payload but also pass through the complex ground such as grass ground, sand ground, mud ground, and so on. ASBs used as brakes help SRWCR to move on inclined surfaces. In addition, SRWCR with capable of both linear and turning locomotion has the potential to navigate through obstacles in confined spaces. In this section, we will discuss the capabilities of SRWCR in terms of the payload, passing capability, obstacle navigation, and so on.

5.1. Payload

Robots are usually designed to perform some functions such as surveillance, search, and rescue, which inevitably require the robot to carry some equipment. Therefore, a large payload is necessary for the robot in practical applications.

We conducted experiments to study the payload capability of the robot. The same experimental setup in Fig. 2 was employed here to measure the speed of the robot under different payloads. The pressures supplied to SPAs and ASBs were adjusted to 0.2 and 0.08 MPa, respectively. The actuation period of SRWCR was set to 1.2 s. The customized lead blocks with a mass of 100 g as a payload were evenly placed in the rigid head and tail of SRWCR, as shown in the inset of Fig. 11. The payload was increased at a step of 200 g. At each payload, SRWCR crawled from the green start line to the red finish line with a distance of 500 mm. Three trials were conducted under the same conditions to calculate the average crawling speed of SRWCR to reduce the measurement error. When the payload increased to 2 kg, because there was no extra space in the rigid head and tail to place more lead blocks, the payload could not continue to increase. Supplementary Movie S6 shows the crawling process at the payload of 2 kg. The experimental results are shown in Fig. 11.

As shown in Fig. 11, the crawling speed of SRWCR decreases with the increase of the payload. There are two main reasons: (1) the friction forces between the wheels and the ground increase as the payload

https://doi.org/10.1017/S0263574722000686 Published online by Cambridge University Press

Table III. *Comparison of the payload capability of our robot with existing soft crawling robots.*

Soft crawling robot	Actuation method	Payload (g)	Speed under payload (mm/s)
Our robot	Pneumatic	2000	11.18
Qin et al. [19]	Vacuum	2000	∼8.2
Li et al. [24]	DE	∼15	∼2
Must et al. [40]	IEAP	∼1.5	∼0.53

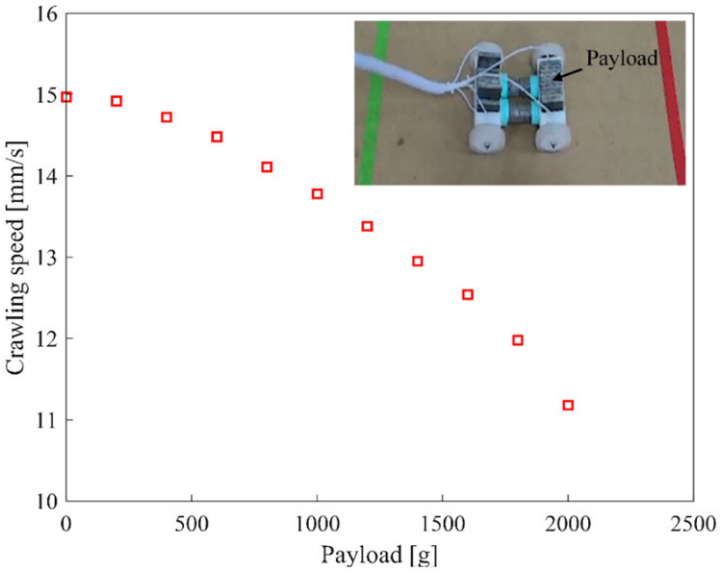

Figure 11. *The speed of SRWCR under different payloads.*

increases, which limits the deformation of the two SPAs, and (2) because the centers of gravity of the rigid head and tail are not in the same plane as the axes of the two SPAs, after SPAs are extended, the rigid head and tail turn around the corresponding wheel shafts to bend SPAs, which reduces the extension length of SPAs and can be observed in Supplementary Movie S6. The bending angle of SPAs increases with the increase of the payload. In addition, when the payload increases to 2 kg, the crawling speed decreases to 11.18 mm/s, which indicates that the payload of SRWCR is far from the maximum. The great payload capability reveals the potential for the development of an untethered crawling robot, which can achieve autonomous operations in practical applications.

Table III compared the payload capability of our robot with existing soft crawling robots. It is shown that only the soft crawling robots developed by Qin et al. [19] can reach the payload of 2 kg. However, our robot has a higher crawling speed under this payload. In addition, compared with other soft crawling robots shown in Table III, our robot not only has the largest payload but also has the largest crawling speed under the corresponding payload, which demonstrates the large payload capability of our robot. The large payload capability of our robot mainly lies in the use of the soft-rigid body. Compared with the purely soft crawling robots, the soft-rigid body of our robot can carry a larger weight without deformation which may cause the robot to fail.

5.2. Passing capability

In addition to moving on flat ground discussed earlier, functional robots such as inspection robots, rescue robots, and search robots often need to pass through some complex grounds such as grass ground, sand

https://doi.org/10.1017/S0263574722000686 Published online by Cambridge University Press

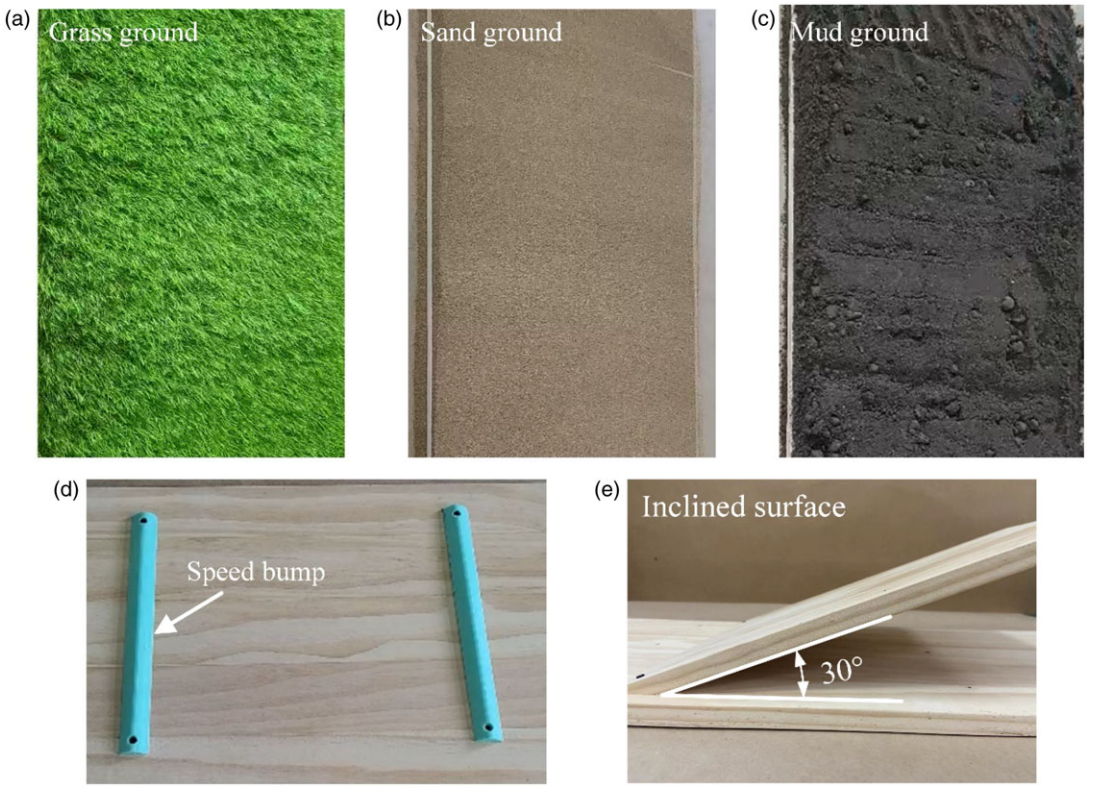

Figure 12. *Construction of a variety of complex grounds, including (a) grass ground, (b) sand ground, (c) mud ground, (d) speed bump, and (e) inclined surface.*

ground, mud ground, speed bump, and inclined surface. Therefore, the robot should have a high passing capability to achieve different functions.

To demonstrate the capability of SRWCR to pass through the complex grounds, a variety of complex grounds were built in Fig. 12. As shown in Fig. 12(a)–(c), the turf, sand, and mud were spread on the rectangular planks to build grass ground, sand ground, and mud ground, respectively. Two speed bumps fabricated by 3D printing were glued on the planks in Fig. 12(d). Besides, a 30° inclined surface was fixed on the planks in Fig. 12(e). Then, we conducted experiments to verify that SRWCR could crawl through the complex grounds shown in Fig. 12. The experimental setup is the same as the experimental setup shown in Fig. 2. The pressures supplied to SPAs and ASBs were adjusted to 0.2 and 0.08 MPa, respectively. The actuation period of SRWCR was set to 1.2 s. The crawling processes of SRWCR on the complex ground were recorded by a camera (Supplementary Movies S7 and S8). The snapshots of the crawling processes on the complex ground are shown in Fig. 13. The experimental results show that SRWCR can crawl through not only the flat ground but also the grass ground, sand ground, mud ground, and speed bump, as shown in Fig. 13(a)–(d). In addition, SRWCR can crawl on a 30° inclined surface, as shown in Fig. 13(e).

In addition to crawling through the single complex ground, another experiment has been carried out to verify that SRWCR can crawl through various complex ground simultaneously. As shown in Fig. 14, a mixed complex ground has been built by connecting grass ground, sand ground, mud ground, and speed bump in sequence. Supplementary Movie S9 shows the crawling processes of SRWCR on the mixed complex ground. The snapshots of the crawling processes on the mixed complex ground are shown in Fig. 15. The experimental result shows that SRWCR can easily crawl through the mixed complex ground. The crawling test of SRWCR on the single complex grounds and mixed complex ground proves the high passing capability of SRWCR.

https://doi.org/10.1017/S0263574722000686 Published online by Cambridge University Press

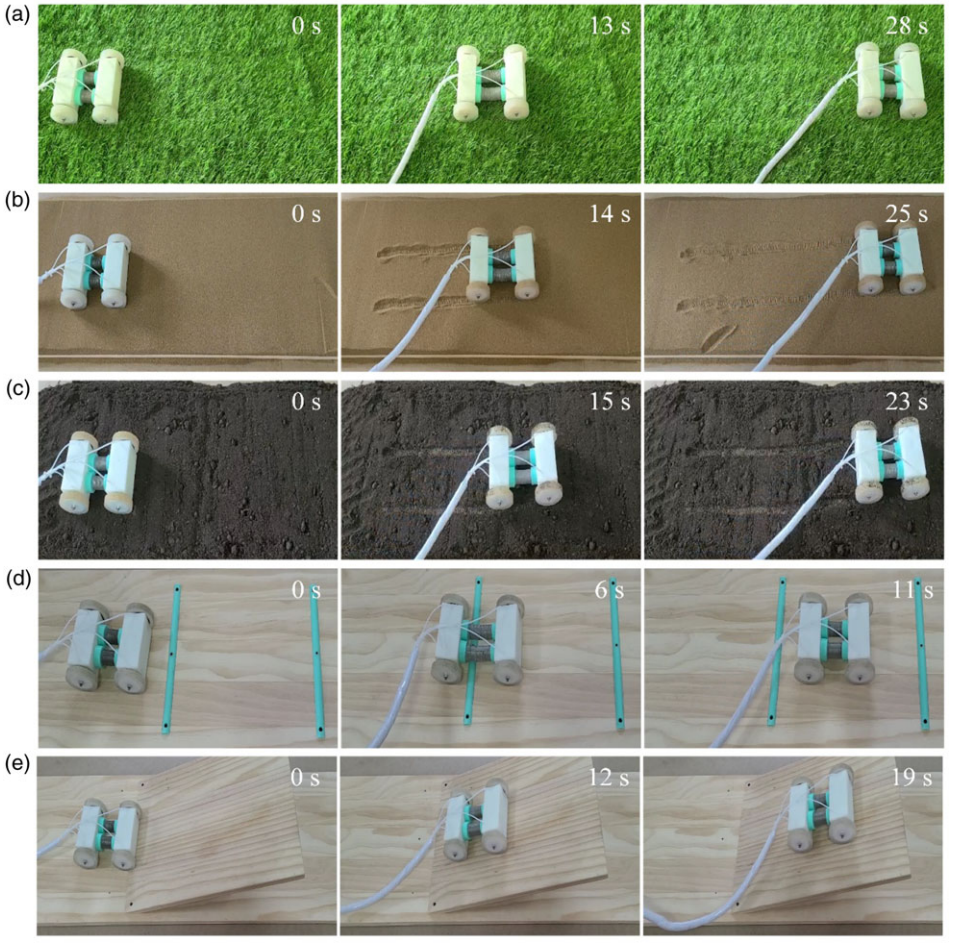

Figure 13. *The image snapshots of SRWCR crawling through a variety of complex grounds, including (a) grass ground, (b) sand ground, (c) mud ground, (d) speed bump, and (e) inclined surface.*

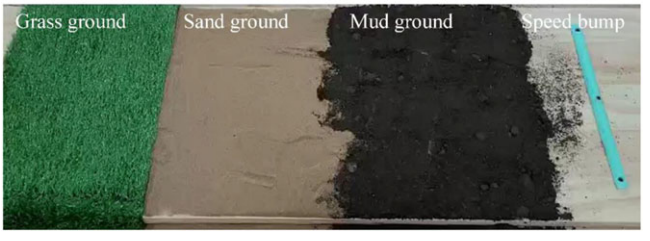

Figure 14. *Connecting the grass ground, sand ground, mud ground, and speed bump to construct a mixed complex ground.*

Table IV shows a comparison of the passing capability of soft crawling robots. As shown in Table IV, only our robot is able to crawl through a variety of complex ground such as the grass ground, sand ground, mud ground, speed bump, and inclined surface. Also, only our robot can crawl through the mixed complex ground described earlier. Compared with the soft crawling robot in Table IV, the use of wheels as the feet of our robot greatly improves the passing capability of our robot. Benefit from the

https://doi.org/10.1017/S0263574722000686 Published online by Cambridge University Press

Table IV. *Comparison of the passing capability of our robot with existing soft crawling robots.*

Soft crawling robot	Actuation method	Wheeled structure	Crawling ground	Crawling on mixed ground
Our robot	Pneumatic	Yes	Flat ground, grass ground, sand ground, mud ground, speed bump, and inclined surface	Yes
Chen et al. [12]	Pneumatic	No	Flat ground	No
Jiang et al. [37]	Pneumatic	No	Flat ground	No
Ge et al. [38	Pneumatic	No	Flat ground and inclined surface	No
Qin et al. [19]	Vacuum	No	Flat ground and inclined surface	No
Umedachi et al. [13	Tendon-driven	No	Flat ground	No
Liang et al. [20]	SMA	No	Flat ground	No
Tang et al. [39]	Nickel wire	No	Flat ground	No
Cao et al. [23]	DE	No	Flat ground	No
Must et al. [40]	IEAP	No	Flat ground and inclined surface	No

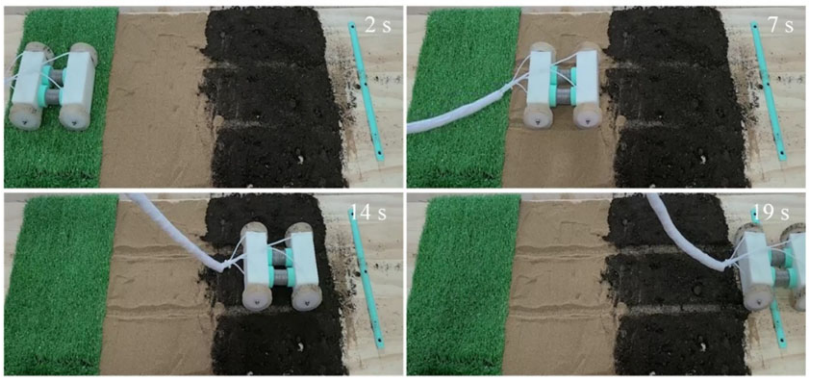

Figure 15. *The image snapshots of SRWCR crawling through the mix complex ground.*

high passing capability, our robot also has high environmental adaptability, which makes it have high potential to be used as the functional robots such as the search and rescue robot.

5.3. Obstacle navigation

To demonstrate the mobility of the robot in confined spaces, we drove SRWCR to navigate through three obstacles by following a figure-of-eight path. The gap distance between two adjacent obstacles is 150 mm, which equals the turning diameter of SRWCR. Figure 16 shows the captured images of the robot at different time steps. SRWCR first rotates around the first obstacle anticlockwise and then changes its direction to rotate around the second obstacle clockwise. Finally, SRWCR returned to the starting position by rotating around the first obstacle anticlockwise again. Due to the fast movement speed, SRWCR managed to complete this task in 129 s. A video of this obstacle navigation is available in Supplementary Movie S10.

https://doi.org/10.1017/S0263574722000686 Published online by Cambridge University Press

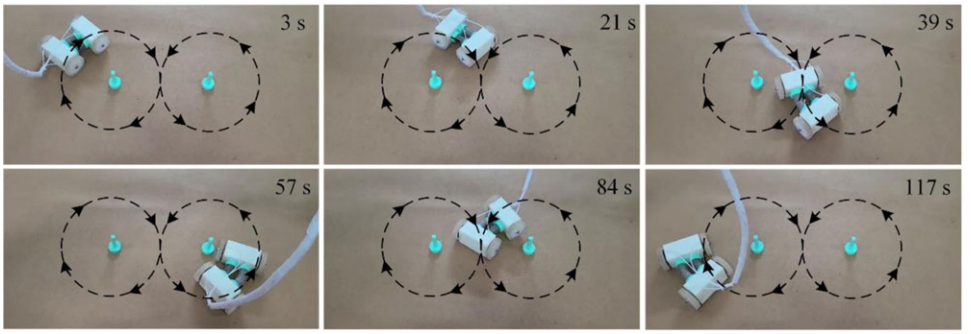

Figure 16. *SRWCR navigates through two obstacles by following a figure-of-eight path.*

6. Conclusion

In this paper, we developed a SRWCR actuated by two extended SPAs and four ASBs. Benefit from the waterproof and fast deformation response of SPA and ASB, SRWCR can achieve an excellent locomotion performance in amphibious environment. Furthermore, compared with the pure soft crawling robots which achieve locomotion through the mechanism of asymmetric friction [25, 41] or using the adsorption-type actuators as their feet, [19, 23, 42] the high payload capability of the soft-rigid body and high passing capability of the wheeled structure make the designed SRWCR have high payload and passing capability. Meanwhile, the soft-rigid body and wheeled structure provide a design method for soft crawling robots with high payload and passing capability. In addition, SRWCR can also achieve obstacle navigation in confined space, which demonstrates the potential advantage of SRWCR in the design of functional robots such as search and rescue robot.

Despite these impressive functionalities, the current soft robot still has many aspects that can be improved. First, our current soft robot requires external air supply device and controller, which greatly limits its functionalities, especially in practical applications. Hence, we plan to develop a fully untethered soft robot with the air supply device and controller on board. Second, we will further verify the payload and passing capability of SRWCR in the actual environment, which is only at the laboratory verification stage now. Third, we plan to further enhance the passing capability of SRWCR from the aspects of structure design to satisfy the needs of performing tasks in an unstructured environment. Fourth, by using the pressure reducing value that can be automatically controlled, the extension length and turning radius of SRWCR can be adjusted, then, the control of SRWCR will be further studied.

Acknowledgments. This work was supported by China Agriculture Research System of MOF and MARA, and the National Natural Science Foundation of China under Grant No. 51975537.

Conflict of interest. The authors confirm that this work is original and has not been published or is under consideration anywhere else. The authors declare that they have no relevant or material financial interests that relate to the research described in this paper. All authors have seen the paper and agree to publish it here.

Supplementary materials. To view supplementary material for this article, please visit https://doi.org/10.1017/S0263574722000686.

References

[1] S. Davarzani, M. A. Ahmadi-Pajouh and H. Ghafarirad, "Design of sensing system for experimental modeling of soft actuator applied for finger rehabilitation," *Robotica*, 1–21 (2021).

[2] M. Cianchetti, T. Ranzani, G. Gerboni, T. Nanayakkara, K. Althoefer, P. Dasgupta and A. Menciassi, "Soft robotics technologies to address shortcomings in today's minimally invasive surgery: The STIFF-FLOP approach," *Soft Robot.* **1**(2), 122–131 (2014).

[3] K. C. Galloway, K. P. Becker, B. Phillips, J. Kirby, S. Licht, D. Tchernov, R. J. Wood and D. F. Gruber, "Soft robotic grippers for biological sampling on deep reefs," *Soft Robot.* **3**(1), 23–33 (2016).
[4] Z. Wang, R. Kanegae and S. Hirai, "Circular shell gripper for handling food products," *Soft Robot.* **8**(5), 542–554 (2020).
[5] J. D. Greer, T. K. Morimoto, A. M. Okamura and E. W. Hawkes, "A soft, steerable continuum robot that grows via tip extension," *Soft Robot.* **6**(1), 95–108 (2019).
[6] C. Majidi, R. F. Shepherd, R. K. Kramer, G. M. Whitesides and R. J. Wood, "Influence of surface traction on soft robot undulation," *Int. J. Robot. Res.* **32**(13), 1577–1584 (2013).
[7] N. Zhu, H. Zang, B. Liao, H. Qi, Z. Yang, M. Chen, X. Lang and Y. Wang, "A quadruped soft robot for climbing parallel rods," *Robotica* **39**(4), 686–698 (2021).
[8] Z. Tang, J. Lu, Z. Wang, G. Ma, W. Chen and H. Feng, "Development of a new multi-cavity pneumatic-driven earthworm-like soft robot," *Robotica* **38**(12), 2290–2304 (2020).
[9] Z. Xie, A. G. Domel, N. An, C. Green, Z. Gong, T. Wang, E. M. Knubben, J. C. Weaver, K. Bertoldi and L. Wen, "Octopus arm-inspired tapered soft actuators with suckers for improved grasping," *Soft Robot.* **7**(5), 639–648 (2020).
[10] Y. Sakuhara, H. Shimizu and K. Ito, "Climbing Soft Robot Inspired by Octopus," *IEEE 10th International Conference on Intelligent Systems (IS)* (2020) pp. 463–468.
[11] J. Zou, Y. Lin, C. Ji and H. Yang, "A reconfigurable omnidirectional soft robot based on caterpillar locomotion," *Soft Robot.* **5**(2), 164–174 (2018).
[12] Y. Chen, B. Hu, J. Zou, W. Zhang, D. Wang and G. Jin, "Design and fabrication of a multi-motion mode soft crawling robot," *J. Bionic Eng.* **17**(5), 932–943 (2020).
[13] T. Umedachi, M. Shimizu and Y. Kawahara, "Caterpillar-inspired crawling robot using both compression and bending deformations," *IEEE Robot. Autom. Let.* **4**(2), 670–676 (2019).
[14] A. Hamidi, Y. Almubarak, Y. M. Rupawat, J. Warren and Y. Tadesse, "Poly-Saora robotic jellyfish: Swimming underwater by twisted and coiled polymer actuators," *Smart Mater. Struct.* **29**(4), 045039 (2020).
[15] J. Frame, N. Lopez, O. Curet and E. D. Engeberg, "Thrust force characterization of free-swimming soft robotic jellyfish," *Bioinspir. Biomim.* **13**(6), 064001 (2018).
[16] Y. Almubarak, M. Punnoose, N. X. Maly, A. Hamidi and Y. Tadesse, "KryptoJelly: A jellyfish robot with confined, adjustable pre-stress, and easily replaceable shape memory alloy NiTi actuators," *Smart Mater. Struct.* **29**(7), 075011 (2020).
[17] R. F. Shepherd, F. Ilievski, W. Choi, S. A. Morin, A. A. Stokes, A. D. Mazzeo, X. Chen, M. Wang and G. M. Whitesides, "Multigait soft robot," *P. Natl. Acad. Sci.* **108**(51), 20400–20403 (2011).
[18] M. T. Tolley, R. F. Shepherd, B. Mosadegh, K. C. Galloway, M. Wehner, M. Karpelson, R. J. Wood and G. M. Whitesides, "A resilient, untethered soft robot," *Soft Robot.* **1**(3), 213–223 (2014).
[19] L. Qin, X. Liang, H. Huang, C. K. Chui, R. C.-H. Yeow and J. Zhu, "A versatile soft crawling robot with rapid locomotion," *Soft Robot.* **6**(4), 455–467 (2019).
[20] S. Shakiba, M. Ayati and A. Yousefi-Koma, "Development of hybrid Prandtl–Ishlinskii and constitutive models for hysteresis of shape-memory-alloy-driven actuators," *Robotica* **39**(8), 1390–1404 (2021).
[21] K. T. Nguyen, S. Y. Ko, J.-O. Park and S. Park, "Terrestrial walking robot with 2DoF Ionic Polymer-Metal Composite (IPMC) legs", *IEEE/ASME T. Mech.* **20**(6), 2962–2972 (2015).
[22] D. Hua, X.-h. Liu, S. Sun, M. Á. Sotelo, Z. Li and W. Li, "A magnetorheological fluid-filled soft crawling robot with magnetic actuation," IEEE/ASME T. Mech **25**(6), 2700–2710 (2020).
[23] J. Cao, L. Qin, J. Liu, Q. Ren, C. C. Foo, H. Wang, H. P. Lee and J. Zhu, "Untethered soft robot capable of stable locomotion using soft electrostatic actuators," *Extreme Mech. Lett.* **21**(5), 9–16 (2018).
[24] T. Li, Z. Zou, G. Mao, X. Yang, Y. Liang, C. Li, S. Qu, Z. Suo and W. Yang, "Agile and resilient insect-scale robot," *Soft Robot.* **6**(1), 133–141 (2019).
[25] X. Lu, K. Wang and T. Hu, "Development of an annelid-like peristaltic crawling soft robot using dielectric elastomer actuators," *Bioinspir. Biomim.* **15**(4), 046012 (2020).
[26] X.-Y. Guo, W.-B. Li, Q.-H. Gao, H. Yan, Y.-Q. Fei and W.-M. Zhang, "Self-locking mechanism for variable stiffness rigid–soft gripper," *Smart Mater. Struct.* **29**(3), 035033 (2020).
[27] Y. Su, Z. Fang, W. Zhu, X. Sun, Y. Zhu, H. Wang, K. Tang, H. Huang, S. Liu and Z. Wang, "A high-payload proprioceptive hybrid robotic gripper with soft origamic actuators," *IEEE Robot. Autom. Let.* **5**(2), 3003–3010 (2020).
[28] W. Li, Z. Li, Y. Liu, L. Ding, J. Wang, H. Gao and Z. Deng, "Semi-Autonomous bilateral teleoperation of six-wheeled mobile robot on soft terrains," *Mech. Syst. Signal Pr.* **133**(9), 106234 (2019).
[29] A. Almusa, R. Galeza, M. Wang and C. Majidi, "Compliance-Tuning Soft Inflatable Wheels for Robot Mobility on Various Terrains," 3rd IEEE International Conference on Soft Robotics (RoboSoft) (2020) pp. 558–563.
[30] J. Yao, "Design and motion analysis of a wheel-walking bionic soft robot," *J. Mech. Eng.* **55**(5), 27 (2019).
[31] Z. Shen, H. Zhong, E. Xu, R. Zhang, K. C. Yip, L. L. Chan, L. L. Chan, J. Pan, W. Wang and Z. Wang, "An underwater robotic manipulator with soft bladders and compact depth-independent actuation," *Soft Robot.* **7**(5), 535–549 (2020).
[32] S. Kurumaya, B. T. Phillips, K. P. Becker, M. H. Rosen, D. F. Gruber, K. C. Galloway, K. Suzumori and R. J. Wood, "A modular soft robotic wrist for underwater manipulation," *Soft Robot.* **5**(4), 399–409 (2018).
[33] H. Feng, Y. Sun, P. A. Todd and H. P. Lee, "Body wave generation for anguilliform locomotion using a fiber-reinforced soft fluidic elastomer actuator array toward the development of the eel-inspired underwater soft robot," *Soft Robot.* **7**(2), 233–250 (2019).
[34] P. Cheng, J. Jia, Y. Ye and C. Wu, "Modeling of a soft-rigid gripper actuated by a linear-extension soft pneumatic actuator," *Sensors (Basel)* **21**(2), 493 (2021).

https://doi.org/10.1017/S0263574722000686 Published online by Cambridge University Press

[35] L. Marechal, P. Balland, L. Lindenroth, F. Petrou, C. Kontovounisios and F. Bello, "Toward a common framework and database of materials for soft robotics," *Soft Robot.* **8**(3), 284–297 (2021).
[36] X. Dong, C. Tang, S. Jiang, Q. Shao and H. Zhao, "Increasing the payload and terrain adaptivity of an untethered crawling robot via soft-rigid coupled linear actuators," *IEEE Robot. Autom. Let.* **6**(2), 2405–2412 (2021).
[37] F. Jiang, Z. Zhang, X. Wang, G. Cheng, Z. Zhang and J. Ding, "Pneumatically actuated self-healing bionic crawling soft robot," *J. Intell. Robot. Syst.* **100**(2), 445–454 (2020).
[38] J. Z. Ge, A. A. Calderon, L. Chang and N. O. Perez-Arancibia, "An earthworm-inspired friction-controlled soft robot capable of bidirectional locomotion," *Bioinspir. Biomim.* **14**(3), 036004 (2019).
[39] X. Tang, K. Li, Y. Liu, D. Zhou and J. Zhao, "A soft crawling robot driven by single twisted and coiled actuator," *Sensor. Actuat. A Phys.* **291**(6), 80–86 (2019).
[40] I. Must, F. Kaasik, I. Põldsalu, L. Mihkels, U. Johanson, A. Punning and A. Aabloo, "Ionic and Capacitive Artificial Muscle for Biomimetic Soft Robotics," *Adv. Eng. Mater.* **17**(1), 84–94 (2015).
[41] E. B. Joyee and Y. Pan, "A fully three-dimensional printed inchworm-inspired soft robot with magnetic actuation," *Soft Robot.* **6**(3), 333–345 (2019).
[42] Y. Tang, Q. Zhang, G. Lin and J. Yin, "Switchable adhesion actuator for amphibious climbing soft robot," *Soft Robot.* **5**(5), 592–600 (2018).

Cite this article: J. Jia, P. Cheng, Y. Ye, Q. Xie and C. Wu (2022). "A novel soft-rigid wheeled crawling robot with high payload and passing capability", Robotica **40**, 3930–3951. https://doi.org/10.1017/S0263574722000686